

# A Bayesian Approach Study of Hybrid Neutron Stars

Fábio Köpp <sup>1,\*</sup> César H. Lenzi <sup>2,†</sup> César V. Flores <sup>3,4,‡</sup> and Débora P. Menezes <sup>1,§</sup>

<sup>1</sup>*Departamento de Física - CFM, Universidade Federal de Santa Catarina, 88.040-900, Florianópolis/SC, Brazil*

<sup>2</sup>*Departamento de Física e Laboratório de Computação Científica Avançada e Modelamento (Lab-CCAM), Instituto Tecnológico de Aeronáutica, DCTA, 12228-900, São José dos Campos/SP, Brazil*

<sup>3</sup>*Centro de Ciências Exatas, Naturais e Tecnológicas, Universidade Estadual da Região Tocantina do Maranhão, 65901-480, Imperatriz/MA, Brazil*

<sup>4</sup>*Departamento de Física - CCET, Universidade Federal do Maranhão, Campus Universitário do Bacanga, 65080-805, São Luís/MA, Brazil*

In this work, we explore how astronomical observations (specifically measurements of masses, radii, and tidal deformabilities) can constrain the presence of quark matter inside neutron stars, namely the phase transition from nuclear matter to deconfined quark matter. Our approach employs Bayesian analysis to study this phenomenon. Hadronic matter is modeled using the relativistic mean-field (RMF) approximation, for which we have selected two parameter sets:  $NL3^*\omega\rho$ , representing hadronic matter with nucleons only, and  $EL3\omega\rho$  with nucleons only and  $EL3\omega\rho Y$ , which includes hyperons. On the other hand deconfined quark matter is modeled using the vector-MIT bag model. For our purpose, the phase transition is implemented using the Maxwell construction. Bayesian inference is performed by tuning three parameters: the bag constant (i.e.  $B^{1/4}$ ), the vector coupling constant ( $G_v$ ), and the Dirac sea contribution ( $b_4$ ). We found that a phase transition could exist at densities below  $2.0n_0$  for both the  $EL3\omega\rho - EL3\omega\rho Y$  and  $NL3^*\omega\rho$  parametrizations. As a consequence, our results also indicate that a hybrid neutron star could have a large quark core that comprises more than 80% of its size.

## I. INTRODUCTION

A neutron star (NS) is one of the most fascinating astrophysical objects in the universe. This compact object is well known for hosting some of the most extreme conditions in nature; for example it exhibits intense magnetic fields, high rotation speeds, and extreme gravitational forces and baryonic densities. At these extreme densities, it is theorized that hadronic nuclear matter could undergo a phase transition to a deconfined strange quark matter, making the existence of hybrid stars possible. The internal structure of a hybrid star can present an outer hadronic layer and a core composed of deconfined quark matter. In this respect, it is of vital importance to study the astrophysical signatures that could reveal the presence of quark matter at the interior of these compact objects.

Advanced terrestrial and space-based instruments are already making significant contributions to the study of compact stars. In particular, the LIGO/Virgo collaboration has detected gravitational waves from neutron star mergers [1], and the Neutron Star Interior Composition Explorer (NICER) has observed neutron star properties through soft X-ray timing [2–4]. These observatories are providing an increasing amount of quantitative data on

key neutron star characteristics such as mass, radius, moment of inertia, and tidal deformability. Such data are crucial for distinguishing between different types of compact stars, hadronic stars, pure quark stars, and hybrid stars, by analyzing these observable properties.

As it is well known, quark matter must be described by Quantum Chromodynamics (QCD), the fundamental theory governing strong interactions. However, an ab initio description of dense matter, whether hadronic or quark, cannot yet be derived directly from QCD. As a result, the quest for an effective model that can accurately represent the neutron star equation of state (EoS) remains a complex and active area of research, with numerous approaches proposed in the literature. To constrain the modeling of dense matter EoS, researchers employ various strategies, including experimental data on symmetric nuclear matter, results from lattice QCD and chiral effective field theory, as well as model-independent EoS fitting techniques [5].

In this context, Bayesian methods have become increasingly popular for exploring the parameter space of high-density nuclear matter models [6–8], as they provide a powerful framework for analyzing neutron star equations of state. These methods combine prior knowledge with observational data to generate probabilistic constraints on key EoS parameters. For example, for the vector MIT bag model these parameters are  $(B^{1/4}, G_v, b_4)$ . In this work, the deconfined quark phase is modeled using the vector MIT bag model, which is discussed in more detail in Section II. The phase transition from hadronic to quark matter is treated using the Maxwell construction [9]. This approach not only refines viable EoS models,

\* [fabio.kopp@proton.me](mailto:fabio.kopp@proton.me)

† [chlenzi@ita.br](mailto:chlenzi@ita.br)

‡ [cesar.vasquez@uemasul.edu.br](mailto:cesar.vasquez@uemasul.edu.br)

§ [debora.p.m@ufsc.br](mailto:debora.p.m@ufsc.br)

but also quantifies the uncertainties in their parameters.

## II. MICROPHYSICS

As mentioned in the Introduction, a hybrid star consists of a core of quark matter surrounded by an outer layer of hadronic matter. Due to the uncertain nature of matter at extremely high densities, the equation of state (EOS) is typically derived using phenomenological models that aim to capture the expected properties of matter across different density regimes. To this end, the deconfined quark matter in the core can be described using the vector MIT bag model (vMIT) [10], while the hadronic outer layer is modeled with the relativistic mean field (RMF) hadronic model [11]. The outer crust is represented by the BPS EOS [12]. This section provides a detailed overview of the theoretical microphysical framework used to construct these models.

### A. Hadronic Matter

Hadronic matter is described using the relativistic mean field hadronic model [13], in which the strong interaction between hadrons is mediated by the exchange of virtual mesons. At the Lagrangian density level, the RMF model is expressed as

$$\begin{aligned} \mathcal{L}_{\text{RMF}} = & \sum_b \bar{\psi}_b \left[ \gamma_\mu \left( i\partial^\mu - g_{b\omega}\omega^\mu - g_{b\rho}\frac{\vec{\tau}_b}{2}\vec{\rho}^\mu \right) - m_b^* \right] \psi_b \\ & + \frac{1}{2}\partial_\mu\sigma\partial^\mu\sigma - \frac{1}{2}m_\sigma^2\sigma^2 - \frac{1}{3!}\kappa\sigma^3 - \frac{1}{4!}\lambda\sigma^4 \\ & - \frac{1}{4}\Omega^{\mu\nu}\Omega_{\mu\nu} + \frac{1}{2}m_\omega^2\omega_\mu\omega^\mu - \frac{1}{4}\vec{R}_{\mu\nu}\vec{R}^{\mu\nu} \\ & + \frac{1}{2}m_\rho^2\vec{\rho}_\mu\vec{\rho}^\mu + \Lambda_v g_{N\omega}^2 g_{N\rho}^2 \omega_\mu\omega^\mu \vec{\rho}_\mu\vec{\rho}^\mu, \end{aligned} \quad (1)$$

where the Dirac spinor  $\psi_b$  represents the baryon  $b$  with the effective mass  $m_b^* = m_b - g_{b\sigma}\sigma$ ,  $\vec{\tau}_b$  are the corresponding Pauli matrices. The coupling constants of the mesons  $i = \sigma, \omega,$  and  $\rho$  with the baryon  $b$  are represented by  $g_{bi}$ ,  $m_i$  is the mass of the meson  $i$ ,  $\kappa$  and  $\lambda$  are scalar self-interaction constants and  $\Lambda_v$  is the  $\omega - \rho$  crossing interaction coefficient. The  $b$  sum extends over the baryons  $n, p, \Lambda, \Sigma^-, \Sigma^0, \Sigma^+, \Xi^-,$  and  $\Xi^0$ . The meson field tensors are  $\Omega_{\mu\nu} = \partial_\mu\omega_\nu - \partial_\nu\omega_\mu$ ,  $\vec{R}_{\mu\nu} = \partial_\mu\vec{\rho}_\nu - \partial_\nu\vec{\rho}_\mu - g_\rho(\vec{\rho}_\mu \times \vec{\rho}_\nu)$  and  $\Phi_{\mu\nu} = \partial_\mu\phi_\nu - \partial_\nu\phi_\mu$ . The parameter sets employed in this work are given in Table I, and the nuclear matter saturation properties are given in Table II.

This hadronic model is fitted to finite symmetric nuclear matter at saturation density ( $n_0$ ), satisfying the following bulk properties: the binding energy  $B/A$ , compressibility modulus  $K_0$ , symmetry energy  $S_0$ , and its slope  $L_0$ . The parameterizations employed in this study

are the NL3 $^*\omega\rho$  [14] and the EL3 $\omega\rho$  [15], both sets satisfying the constraints imposed by microscopic calculations of nuclear matter [16]. The presence of hyperons in the EL3 $\omega\rho$  set is also examined. The couplings of hyperons to vector mesons as well as scalar mesons are presented in Appendix A - item B. This parametrization includes the strange isoscalar-vector field  $\phi^\mu$ , which enables the existence of hyperonic stars with masses of approximately  $2 M_\odot$ . It is important to emphasize that EoSs used in this work are both in beta equilibrium and under local charge neutrality [14, 15].

### B. Strange Quark Matter

An important consideration in the high density regime is the strange matter hypothesis, which suggests that strange quark matter (SQM), composed of up, down, and strange quarks may be the true ground state of hadronic matter [17–19].

Studying matter under extreme conditions is challenging due to the complexity of QCD. The two main approaches - lattice QCD (LQCD) and effective models - each have their limitations. For example, LQCD encounters difficulties such as the sign problem and limited applicability at low chemical potentials [20], which makes it unsuitable for investigating high-density matter. Consequently, effective models are commonly used to study matter at high densities, particularly in compact objects like neutron stars. The limitations of relativistic mean-field models, for example, are associated with the requirement that  $r_0 \ll \frac{1}{m_{\text{fields}}}$ , where  $m_{\text{fields}}$  denotes the meson masses. This condition is, however, completely violated both in nuclei and in neutron stars[21].

The MIT bag model posits that each baryon consists of three non-interacting quarks confined within a bag. This bag corresponds to an infinite potential well that confines the quarks [22]. In this simplified model, quarks move freely inside the bag but are prohibited from escaping. The pressure within the bag results from the quarks kinetic energy, which is balanced by the vacuum pressure exerted by the bag itself. Thus, the model captures two key properties of QCD: asymptotic freedom and confinement. In this case the MIT Lagrangian density is given by:

$$\mathcal{L}_{\text{MIT}} = \sum_{u,d,s} \{ \bar{\psi}_q [i\gamma^\mu\partial_\mu - m_q]\psi_q - B \} \Theta(\bar{\psi}_q\psi_q), \quad (2)$$

where  $m_q$  is the  $q$  quark mass,  $\psi_q$  is the Dirac quark field,  $B$  is the constant vacuum pressure and  $\Theta(\bar{\psi}_q\psi_q)$  is the Heaviside step function that is included to assure that the quarks exist only inside the bag.

In this work, we use a variant of the MIT bag model to describe the EoS of deconfined strange quark matter, know as the vector MIT bag model. In this formula-

TABLE I: Parameter sets for the models discussed in the text. The meson masses  $m_\sigma$ ,  $m_\omega$ , and  $m_\rho$  are all given in MeV. The nucleon mass is  $M = 939$  MeV.

Model	$m_\sigma$	$m_\omega$	$m_\rho$	$g_{N\sigma}$	$g_{N\omega}$	$g_{N\rho}$	$\kappa/g_\sigma^3$	$\lambda/g_\sigma^4$	$\Lambda_v$
NL3 $^*\omega\rho$	502.574	782.600	763.000	10.0944	12.8065	14.4410	0.004417	-0.017422	0.045
EL3 $\omega\rho$	512.000	783.000	770.000	9.0286	10.5970	9.4381	0.008280	-0.023400	0.0283

tion, quarks interact via a repulsive vector field analogous to the  $\omega$  meson exchange in relativistic mean-field hadronic models. The lagrangian for this vector interaction is given by

$$\mathcal{L}_V = \sum_{u,d,s} g_V \{ \bar{\psi}_q [\gamma^\mu V_\mu] \psi_q \} \Theta(\bar{\psi}_q \psi_q), \quad (3)$$

we also consider the mass term and the Dirac sea contribution[10],

$$\mathcal{L}_V = \frac{1}{2} m_V^2 V_\mu V^\mu + b_4 \frac{(g_V^2 V_\mu V^\mu)^2}{4}, \quad (4)$$

the mass of the vector field,  $m_V$ , is taken to be 780 MeV, and  $b_4$  is a dimensionless parameter to modulate the Dirac sea contribution.

In this work, the strength of the vector channel is directly related to  $(g_V/m_V)^2$ , so we define

$$G_V = \left( \frac{g_V}{m_V} \right)^2, \quad (5)$$

and adopt  $m_u = m_d = 4$  MeV and  $m_s = 93$  MeV.

To ensure that strange matter remains electrically neutral and in chemical equilibrium, the following equations must be satisfied[10],

The effective chemical potential of the quarks  $\mu_q$  and leptons ( $l$ ) are:

$$\begin{aligned} \mu_q &= \sqrt{m_q^2 + k_q^2} + \left( \frac{g_v}{m_V} \right)^2 n_Q \\ \mu_l &= \sqrt{m_l^2 + k_l^2}. \end{aligned} \quad (6)$$

Then we can use the local charge conservation condition

$$\frac{2}{3} \rho_u - \frac{1}{2} (\rho_d + \rho_s) - \rho_e - \rho_\mu = 0 \quad (7)$$

and the beta equilibrium condition

$$\mu_s = \mu_d = \mu_u + \mu_e, \quad \mu_\mu = \mu_e. \quad (8)$$

respectively.

In equation (6),  $k_q$  denotes the Fermi momentum of the quarks, while  $k_l$  represents the Fermi momenta of electrons and muons. We must emphasize that beta equilibrium and local electric charge conservation must be

maintained even under conditions of strange matter instability - a necessary condition for the stability of the star.

For a stable hybrid star with a quark core, the vMIT model parameters  $\{B^{1/4}, G_v, b_4\}$  must ensure that strange quark matter remains *energetically disfavored* [10, 23]. In other words, the previous parameters must lie outside of the stability window. Otherwise, the entire hadronic layer would convert to deconfined matter, resulting in a strange star rather than a hybrid star [24, 25].

### C. Hadron-Quark Phase Transition

There is a well-documented tension between lattice QCD (LQCD) and effective models regarding the nature of the QCD phase transition. LQCD predicts a smooth crossover transition at low chemical potential, occurring at a temperature of approximately 160–170 MeV [26–28]. In contrast, effective models indicate a first-order phase transition at high densities. Between these regimes, the transition is expected to culminate in a critical end point (CEP), where the phase transition becomes second order [29]. However, the existence and exact location of the CEP remain uncertain [30, 31].

We assume that the hadron-quark deconfinement transition is a first-order phase transition, as predicted by effective models in the high-density region of the QCD phase diagram. It is important to emphasize that the exact properties of the phase transition are model-dependent. The characteristics of the transition depend on the quark and hadron EoS models used. For instance, [32] suggests that, within the Polyakov loop formalism, the onset of the phase transition at zero temperature requires a chemical potential greater than  $\mu = 1050$  MeV.

The thermodynamic description of this process involves matching the EoS of the two phases, and identifying the point of phase coexistence. A first-order phase transition can be obtained in two ways: according to either the Maxwell or Gibbs constructions. In Maxwell construction, the two phases are distinct and maintain local charge conservation. In contrast, the Gibbs construction allows quarks and hadrons to coexist up to a certain baryonic density, with global charge conservation applied. To determine which phase construction to apply, the surface tension serves as the primary criterion for describing the phase transition appropriately. If the surface tension exceeds 60 MeV/fm<sup>2</sup>, the Maxwell con-

TABLE II: Nuclear matter properties for the models discussed in the text. The binding energy  $B/A$ , compressibility modulus  $K_0$ , symmetry energy  $S_0$ , and its slope  $L_0$  are given in MeV, and the effective mass parameter  $M^*/M$  is dimensionless. All quantities are calculated at the saturation density  $n_0$  (in  $\text{fm}^{-3}$ ).

Model	$n_0$	$M^*/M$	$E/A$	$K_0$	$S_0$	$L_0$
NL3 $^*\omega\rho$	0.150	0.59	16.3	258	30.7	42
EL3 $\omega\rho$	0.156	0.69	16.2	256	32.1	66

struction is adequate [33, 34]. Conversely, if it is lower, the Gibbs construction must be preferred. In this study, we choose the Maxwell construction due to the uncertainties surrounding the value of the surface tension [35–38] and the fact that the choice of either Gibbs or Maxwell constructions has a minimal impact on the mass-radius relations of neutron stars.

The thermodynamic description of the Maxwell construction involves matching the EoS for the two phases to determine the phase coexistence point – where  $P_{\text{hadron}} = P_{\text{quark}} = P_0$  (mechanical equilibrium) and  $\mu_{\text{hadron}} = \mu_{\text{quark}} = \mu_0$  (chemical equilibrium). The location of the coexistence point is determined from the equations of state of both the hadronic and the quark phases, so it is expected that the choice of the vector MIT bag model free parameters significantly influences the transition point for a given baryonic composition of the hadronic phase. One can observe that the parameters of hadronic equations of state (EoSs) are fixed. Hence, only the vector MIT bag model exhibits variations in its slope ( $P \times \mu$  plane).

### III. MACROPHYSICS

In this section, we investigate the imprint of different phase transitions on the structure and tidal deformability of hybrid stars. First we present the stellar structure differential equations for an equilibrium compact star. With these equations at hand, it is possible to obtain the mass, radius, and baryonic number. Second, we present the differential equation of tidal deformability, whose results can be compared with recent observations of gravitational waves.

#### A. Stellar structure

The hydrostatic equilibrium configuration of a non-rotating compact star is determined by the Tolman-Oppenheimer-Volkoff (TOV) equations of relativistic stellar structure [39]. In order to obtain those equations, we have to select the following static spherically symmetric metric,

$$ds^2 = -e^\nu dt^2 + e^\lambda dr^2 + r^2(d\theta^2 + \sin^2\theta d\phi^2), \quad (9)$$

in addition, we consider the energy-momentum tensor of a perfect fluid, as given below

$$T_{\mu\nu} = pg_{\mu\nu} + (\epsilon + p)u_\mu u_\nu, \quad (10)$$

where  $\epsilon$ ,  $p$ , and  $u_\mu$  are, respectively, the energy density, pressure, and four-velocity of a fluid element.

Once we have the metric (9) and the energy-momentum tensor (10), we proceed to use these quantities as input for the Einstein field equations(11)

$$R_{\mu\nu} - \frac{1}{2}g_{\mu\nu}R = 8\pi T_{\mu\nu}. \quad (11)$$

After some algebraic work, we can obtain the TOV equations that describe the hydrostatic equilibrium. These equations reads as

$$\frac{dp}{dr} = -\frac{\epsilon m}{r^2} \left(1 + \frac{p}{\epsilon}\right) \left(1 + \frac{4\pi p r^3}{m}\right) \left(1 - \frac{2m}{r}\right)^{-1}, \quad (12)$$

$$\frac{d\nu}{dr} = -\frac{2}{\epsilon} \frac{dp}{dr} \left(1 + \frac{p}{\epsilon}\right)^{-1}, \quad (13)$$

$$\frac{dm}{dr} = 4\pi r^2 \epsilon, \quad (14)$$

$$\frac{dA}{dr} = \frac{4\pi r^2 n_b}{\sqrt{1 - 2m/r}}, \quad (15)$$

where  $p$  is the pressure,  $\epsilon$  is the energy density,  $m$  is the gravitational mass,  $\nu$  is the metric potential,  $A$  is the baryonic number and  $n_b$  is the baryonic number density. The local pressure, energy density and baryonic number density are related by the equation of state previously discussed in section II.

In order to solve the TOV equations, we start the integration at the star center using the following initial conditions  $m(0) = 0$ ,  $A(0) = 0$ ,  $p(0) = p_c$ , where  $p_c$  is the central pressure. The integration is performed until the pressure becomes null and at this point we define radius of the star. We found necessary to comment that the total baryon number is given by equation (15), which is useful to calculate the baryon mass of the star, assuming  $M_B = Am_n$ , where  $m_n$  is the neutron mass. Also considering continuity of the gravitational field, we impose the following matching condition for the metric:  $\nu(R) = \ln(1 - 2M/R)$ .

## B. Tidal Deformability

In a binary system, the shape of each star becomes deformed due to the external tidal field ( $\phi_{ij}$ ) exerted by its companion. As a result, the stars develop a quadrupole moment ( $Q_{ij}$ ), which is linearly proportional to the tidal field, with the proportionality constant represented by  $\lambda$ . This relationship is expressed as:

$$Q_{ij} = -\lambda\phi_{ij}. \quad (16)$$

The dimensionless tidal deformability ( $\Lambda$ ) is connected to the compactness parameter, defined as  $C = M/R$ , through the relation:

$$\Lambda \equiv \frac{\lambda}{M^5} = \frac{2k_2}{3C^5}. \quad (17)$$

The tidal deformability parameter quantifies how easily a compact object—in this case, a hybrid star in a binary system (HS-HS merger)—is deformed under the influence of an external tidal field ( $\phi_{ij}$ ). A larger  $\lambda$  value indicates a more deformable compact object.

Here we provide a summary of the calculation procedure of the dimensionless tidal parameter  $\Lambda$ . One must integrate the following first order differential equation [40–42],

$$r \frac{dy}{dr} + y^2 + yF(r) + r^2Q(r) = 0, \quad (18)$$

where the coefficients  $F(r)$  and  $Q(r)$  are given by

$$F(r) = [1 - 4\pi r^2(\epsilon - p)] \left[1 - \frac{2m}{r}\right]^{-1}, \quad (19)$$

$$Q(r) = 4\pi \left[5\epsilon + 9p + \frac{\epsilon + p}{c_s^2} - \frac{6}{4\pi r^2}\right] \left[1 - \frac{2m}{r}\right]^{-1} - \frac{4m^2}{r^4} \left[1 + \frac{4\pi r^3 p}{m}\right]^2 \left[1 - \frac{2m}{r}\right]^{-2}, \quad (20)$$

with  $\epsilon$ ,  $p$ ,  $m$ , and  $c_s^2 = dp/d\epsilon$  being respectively the energy density, pressure, mass, and the squared speed of sound.

To integrate the differential equation (18), we start at the center of the star with the initial condition  $y(0) = 2$ , using the mass, density, pressure, and speed of sound defined at each point inside the star (these quantities are obtained from the solution of the TOV equations). When the surface of the star is reached we stop the integration and finally get  $y_R$ . This last quantity is used to obtain

the second-order Love number, defined by

$$k_2 = \frac{8C^5}{5} (1 - 2C)^2 [2 - y_R + 2C(y_R - 1)] \times \{2C[6 - 3y_R + 3C(5y_R - 8)] + 4C^3[13 - 11y_R + C(3y_R - 2) + 2C^2(1 + y_R)] + 3(1 - 2C)^2[2 - y_R + 2C(y_R - 1)] \ln(1 - 2C)\}^{-1}. \quad (21)$$

Once  $k_2$  is defined, it is possible to calculate  $\Lambda$ .

Furthermore, in order to calculate the dimensionless tidal deformability of each hybrid star in the inspiral, we use the chirp mass,

$$\mathcal{M} = \frac{(m_1 m_2)^{3/5}}{(m_1 + m_2)^{1/5}} \quad (22)$$

The following values[43] refer to the low-spin prior ( $|\chi| \leq 0.05$ ), as both  $m_1$  and  $m_2$  are consistent with the masses of all known binary neutron star systems[44] with 90% credible intervals.

The chirp mass  $\mathcal{M} = 1.188_{-0.002}^{+0.004} M_\odot$ , with the primary mass  $m_1 \in [1.36, 1.60] M_\odot$ , the secondary mass  $m_2 \in [1.17, 1.36] M_\odot$ , and the total mass  $m_{\text{tot}} = 2.74_{-0.01}^{+0.04} M_\odot$ . The combined dimensionless tidal deformability - to leading order in  $\Lambda_1$  and  $\Lambda_2$  is

$$\bar{\Lambda} = \frac{16}{13} \frac{(m_1 + 12m_2)m_1^4\Lambda_1 + (m_2 + 12m_1)m_2^4\Lambda_2}{(m_1 + m_2)^5}, \quad (23)$$

with  $\bar{\Lambda}$  - assuming a uniform prior - and  $\Lambda(1.4) \leq 800$  for low-spin priors. The probability density shown in the plots of  $\Lambda_1$  against  $\Lambda_2$  should be considered as a conservative upper limit, as the post-Newtonian model tends to overestimate these values[44].

## IV. UNIVERSAL RELATIONS

Universal relations (i.e insensitive to the equation of state) establish a direct link between the microscopic and macroscopic properties of neutron stars, providing valuable understanding of nuclear matter. One way to break the degeneracies in neutron star properties is by using these relations. For instance, the authors of [45] found the binary Love relation. Using individual Love numbers, they constructed a dimensionless symmetric combination

$$\bar{\lambda}_s = \frac{\bar{\lambda}_1 + \bar{\lambda}_2}{2},$$

and a dimensionless antisymmetric combination,

$$\bar{\lambda}_a = \frac{\bar{\lambda}_1 - \bar{\lambda}_2}{2},$$

where  $\bar{\lambda}_A = \lambda_A/m_A^5$ , **and the index  $\mathbf{A}=1,2$** . The relation between  $\bar{\lambda}_s$  and  $\bar{\lambda}_a$  holds for  $q = m_2/m_1 < 1$  and  $m_1 \in (1M_\odot, m_1^{\max})$ , where  $m_1^{\max}$  is the maximum mass of a stable neutron star for a given EoS. The authors verify this relation using the following realistic EOSs: WFF1[46], MS1[47], LS220[48], and AP4[49]. This relation enables the inference of individual tidal deformabilities, which are currently not directly measurable from gravitational wave data. Another relation, such as the Love-C relation [50] between tidal deformability and neutron star compactness, can be used to estimate the neutron star radius. The following relations, which link the moment of inertia, tidal deformability, and quadrupole moment ("I-Love-Q"), are remarkably precise, holding with approximately percent-level accuracy[50]. Furthermore, we utilize an approximately universal relation proposed by the authors [51], which connects  $\Upsilon = \frac{P_c}{\epsilon_c}$  with  $C/\bar{I}/\Lambda$ , where  $C$  represents the compactness of the star,  $\bar{I}$  denotes the dimensionless moment of inertia, and  $\Lambda$  is the dimensionless tidal deformability.  $\Upsilon$  can be interpreted as a mean notion of the stiffness of nuclear matter within the star. It depends on microscopic properties and is defined as the ratio of central pressure to central energy density. We compare our results with the fit, which incorporates 24 realistic hadronic EOSs and one for a hybrid star with a quark core, QHC19. The fit is a fifth-degree polynomial. It should be noted that this fit is only valid for  $C > 0.05$ . We hope that our results fall within the error band of this fit, indicating agreement with these relations. In this way, it is even possible to determine the values of the dimensionless moment of inertia from  $\Upsilon$  with a good approximation.

## V. BAYESIAN INFERENCE METHODOLOGY

Bayesian inference is a robust statistical approach for estimating model parameters from data [6, 52–58]. By applying Bayes' theorem [59], prior knowledge about the parameters is systematically updated in light of new data, resulting in posterior distributions that reflect the refined understanding of these parameters. In this section, we present Bayesian analysis as a tool for constraining the vMIT model parameters and, consequently, the onset of deconfined quark matter.

The main idea is to construct the posterior probability distribution of the model parameters via the Bayes' Theorem, which reads as

$$P(\theta|D, M) = \frac{P(D|\theta, M)P(\theta, M)}{P(D, M)}. \quad (24)$$

This approach allows for the calculation of the probability distribution of a set of parameters  $\theta$ , given the data  $D$  within a specific model  $M$ . The resulting distribution,  $P(\theta | D, M)$ , is known as the posterior probability. It is derived by combining prior knowledge, represented by

TABLE III: Mass, radius and tidal deformability of the compact stars used as constraints in the likelihood function.

Star	Mass [ $M_\odot$ ]	Radius [km]	$\Lambda$
PSR J0740+6620 [2]	$2.072^{+0.067}_{-0.066}$	$12.39^{+1.30}_{-0.98}$	-
PSR J0030+0451 [60]	$1.34^{+0.15}_{-0.16}$	$12.71^{+1.14}_{-1.19}$	-
GW170817 (m1) [1, 44]	$1.46^{+0.12}_{-0.10}$	$10.8^{+2.0}_{-1.7}$	-
GW170817 (m2) [1, 44]	$1.27^{+0.09}_{-0.09}$	$10.7^{+2.1}_{-1.5}$	-
GW170817 ( $\Lambda$ ) [44]	1.4	-	$190^{+390}_{-120}$

the prior probability  $P(\theta, M)$ , which reflects the understanding before accounting for the data, with the likelihood function  $P(D | \theta, M)$ , which represents the statistical information derived from probabilistic models. The probability of the observed data  $D$ , known as the evidence  $P(D, M)$ , serves as a normalization factor since it does not depend on the parameters.

For the inference performed in this study we have the vMIT model parameters being  $\theta = \{B^{1/4}, G_v, b_4\}$  and assume an uniform prior distribution within the ranges  $B^{1/4} \in [150, 180]$  MeV,  $G_v \in [0.2, 0.3]$  fm<sup>2</sup> and  $b_4 \in [0, 2]$ . The data set  $D$  are the masses, radii and dimensionless tidal deformability, as presented in Table III. For the likelihood function we have assumed the Gaussian distribution

$$P(D|\theta, M) = \prod_i \frac{1}{\sqrt{2\pi\sigma_i^2}} e^{-\frac{1}{2}\left(\frac{d_i - m_i(\theta)}{\sigma_i}\right)^2} \quad (25)$$

where  $m_i(\theta)$  correspond to the resulting hybrid star quantity for the model with the parameter set  $\theta$ , and  $d_i$  is the respective quantity data value. We assume that the uncertainty  $\sigma_i$  for each case is determined by the highest observational data uncertainty provided, except for GW170817 ( $\Lambda_{1.4}$ ), for which the lowest uncertainty is assumed. The index  $i$  runs over all the data-points considered (see Table III). We utilize the `emcee` Python package [61] to perform Markov Chain Monte Carlo (MCMC) posterior sampling. The `corner` Python package[62] is utilized to create contour plots, while other plots are generated using Gnuplot[63].

## VI. RESULTS AND DISCUSSION

In this section, we analyze the results from Bayesian inference for the vMIT parameter set for the hadronic parameter sets  $NL3^*\omega\rho$ ,  $EL3\omega\rho$  and with hyperons  $EL3\omega\rho Y$ . It is worth mentioning that the parameter set  $NL3^*\omega\rho$  results in a stiff EoS, while  $EL3\omega\rho$  leads to an intermediate EoS. In this way, by applying the Maxwell construction and Bayesian inference with the aforementioned priors and likelihood distribution, we aim to determine the best vMIT set  $H(G_v, B^{1/4}, b_4)$ . Next, H2 denotes the use of two parameters in the vMIT model, i.e.,  $H2(G_v, B^{1/4})$ , while H3 denotes the use of three parameters, i.e.,  $H3(G_v, B^{1/4}, b_4)$ . that most accurately de-

scribes both astronomical observations and gravitational wave detections through the dimensionless tidal deformability.

We separate the results by baryonic density number. For the first set of results, we do not impose any constraint on the baryonic density number. The following results correspond to the  $EL3\omega\rho$  set.

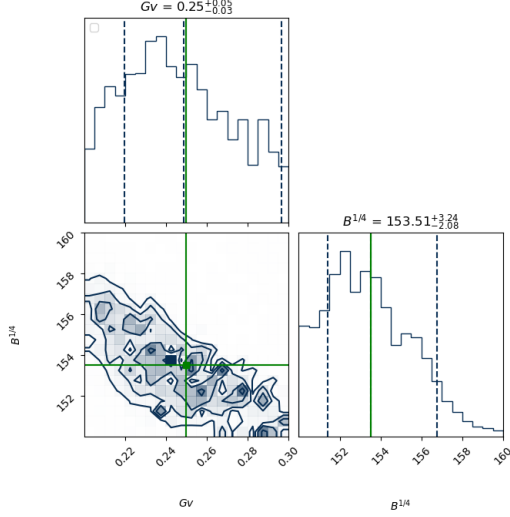


FIG. 1: The results for the inference on two vMIT parameters with H2(0.25, 153.51).

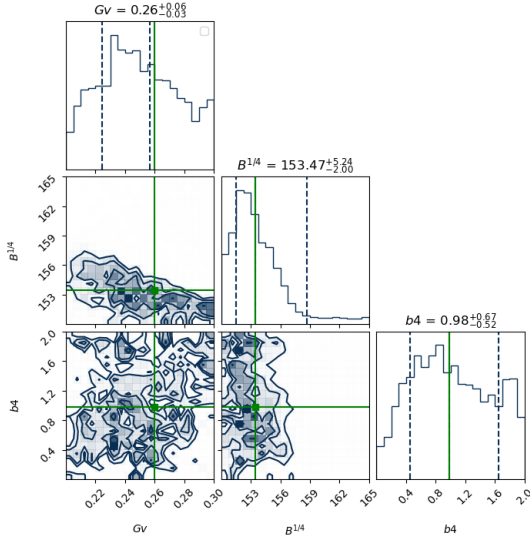


FIG. 2: The case for three vMIT parameters with H3(0.26, 153.47, 0.98).

The dark to light contours in Fig. 1 and Fig. 2 represent the  $1\sigma$ ,  $2\sigma$ , and  $3\sigma$ , respectively. The dashed vertical lines in the histograms represent the 0.16, 0.5, and 0.84 quantiles. The green solid line represents the inferred median value.

In Fig. 4, it is possible to observe that the inferred parameters, considering two or three parameters, yield al-

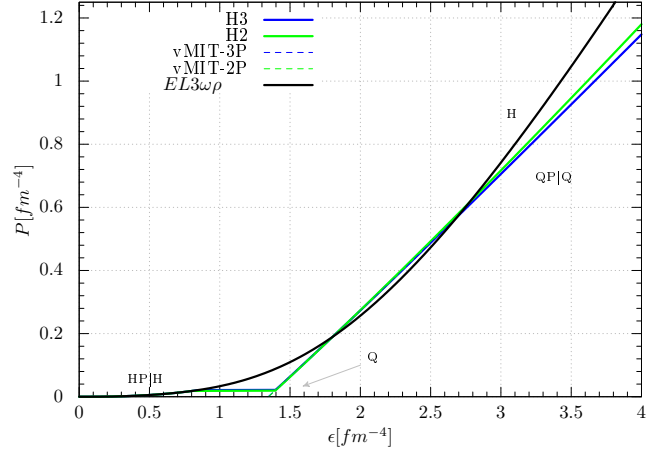


FIG. 3: The plot shows the EoS for the parameter set  $EL3\omega\rho$  and vMIT with two and three parameters, along with their corresponding hybrid star, H2(0.25, 153.51) and H3(0.26, 153.47, 0.98). We also indicate the phases as HP for the hadron phase and QP for the quark phase.

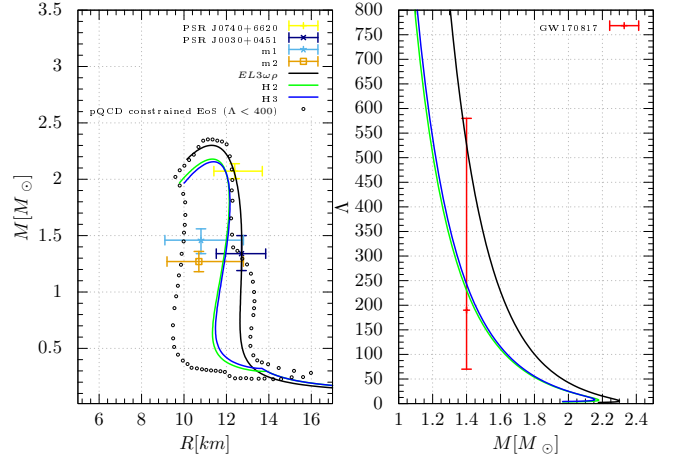


FIG. 4: The left plot shows the mass-radius diagram for the vMIT inference values for the parameter set  $EL3\omega\rho$  set. The right plot the results for  $\Lambda$  against  $M_\odot$ .

most the same results for both the mass-radius relations and the dimensionless tidal deformability. They are in good agreement with the observed data from the Table III. The open-dots - pQCD constrained EoS ( $\Lambda < 400$ ) - indicates the constraint obtained by the authors [64]. The area indicated by the open dots is generated by considering the EOS given by Chiral Effective Field Theory ( $\chi EFT$ ) for densities up to  $n = 1.1n_0$ , since its uncertainties at this density reach  $\pm 24\%$ . The advantage of  $\chi EFT$  lies in its ability to estimate errors for its predictions at each loop calculation and explain the hierarchy of two, three, and weaker higher-body forces [65]. They employed the "hard" or "soft" EoS from Ref. [65], which correspond to the most extreme EoS permitted at low densities. For the intermediate densities, it was used the polytropic form  $p_i = k_i n^{\gamma_i}$  with three or four polytropes up to  $\mu_B = 2.6 GeV$  - with uncertainty level of  $\pm 24\%$ .

Both  $k$  and  $\gamma$  (adiabatic index) are constants determined for each range density (index  $i$ ) of the EoS. This chemical baryon potential corresponds to the deconfined quark matter at high density ( $40n_0$ ) obtained from the calculation of NNLO pQCD[66]. Thus, the open dots correspond to the previous EoS for 4 tropes, which can describe both the GW170817 event and the 2 solar mass constraints. The plot on the left of Fig. 4 for the parameter set  $EL3\omega\rho$  indicates good agreement with the previous constraint and with the observational data in Table III. However, the beginning of the phase transition is almost at the saturation density, which might be interpreted as unphysical.

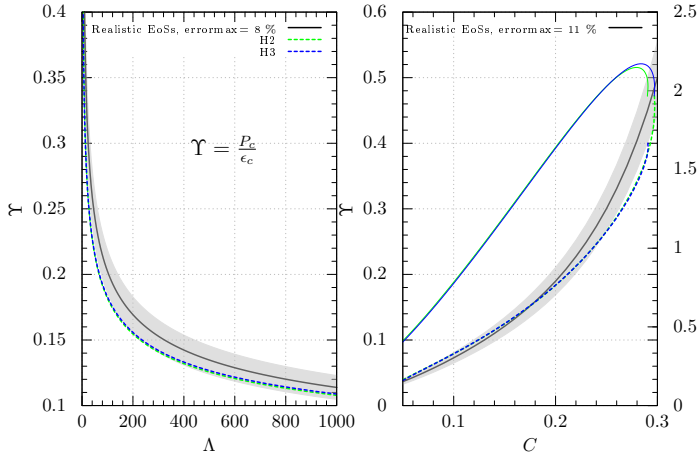


FIG. 5: The approximately universal relation for both  $\Upsilon - \Lambda$  and  $\Upsilon - C$  [51].

In the Fig. 5, one can note on the left plot that the two sets H2 and H3 for  $\Upsilon$  are practically the same and for  $\Lambda > 120$  they are within the error margin. However, on the right plot, the  $\Upsilon$  in terms of  $C$  is shown. To estimate the dimensionless moment of inertia from  $\Upsilon$ , we should use only the values for  $C < 0.25$ , as these lie within the error band.

Presented below are the results corresponding to the parameter set  $NL3^*\omega\rho$ .

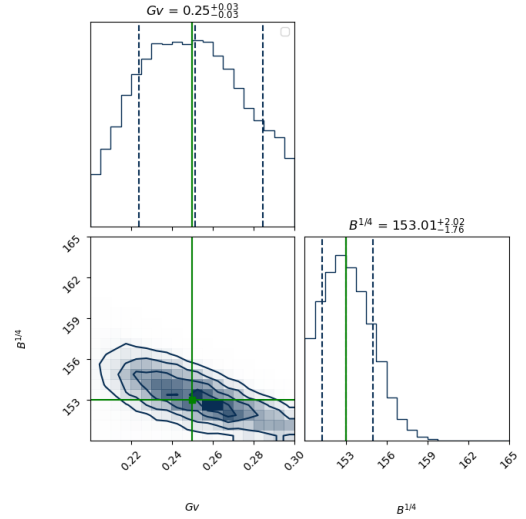


FIG. 6: The same plot as Fig. 1, but for the  $NL3^*\omega\rho$  with H2(0.25, 153.01).

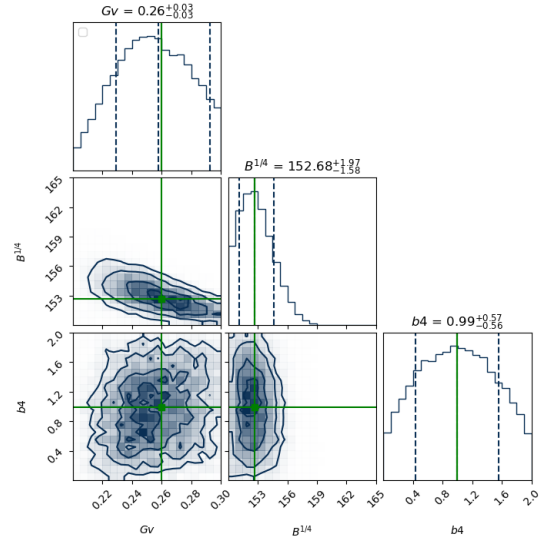


FIG. 7: The same plot as Fig. 6, but for the  $NL3^*\omega\rho$  with H3(0.26, 152.68, 0.99).

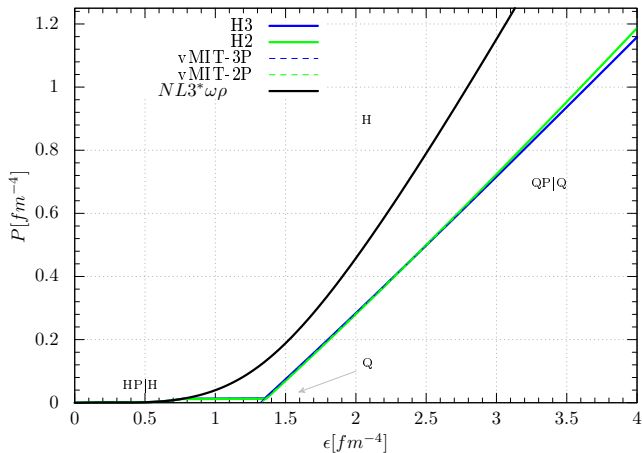


FIG. 8: The same plot as in Fig. 3, but corresponding to the parameter set  $NL3^*\omega\rho$  with  $H2(0.25, 153.01)$  and  $H3(0.26, 152.68, 0.99)$ .

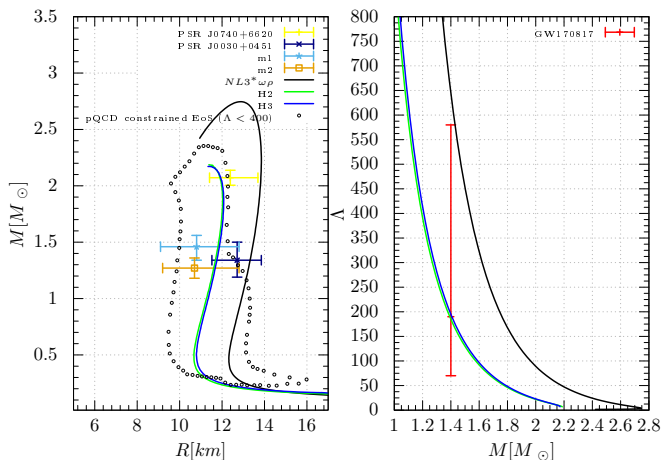


FIG. 9: The same plot as in Fig. 4, but corresponding to the parameter set  $NL3^*\omega\rho$ .

The mass-radius relations for  $H2(0.25, 153.01)$  and  $H3(0.26, 152.68, 0.99)$  in Fig. 9 on the left are in agreement with the observational data from Table III. The  $NL3^*\omega\rho$  parametrization is not in agreement with the  $\chi EFT$  constraints, i.e., for low star mass. Nevertheless, the dimensional tidal deformability for both sets is exactly over the median value for  $1.4 M_\odot$  of GW170817 event. We should emphasize that our results take into account only the observational data from Table III.

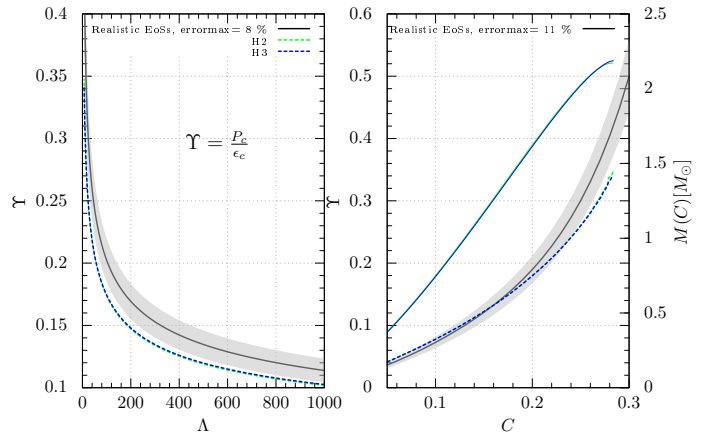


FIG. 10: The same plot as in Fig. 5, but corresponding to the parameter set  $NL3^*\omega\rho$ .

The left plot in Fig. 10, i.e., the  $\Upsilon - \Lambda$  relation for the two sets, is completely outside the error band. Consequently, we disregard the usefulness of this relation for both sets.

In Table IV, we present the following parameters related to the beginning of the phase transition: baryon density number ( $n_b$ ), critical pressure ( $P_{\text{critical}}$ ), the width of the phase transition in terms of energy density ( $\Delta\varepsilon$ ), and the critical baryon chemical potential ( $\mu_{\text{critical}}$ ).

The values obtained for the set with two or three parameters, considering different nuclear EoS, are very close to each other. Recall that the nuclear parametrization set  $EL3\omega\rho$  can be assumed as an intermediate EoS, while  $NL3^*\omega\rho$  corresponds to a stiff EoS.

There are two caveats regarding our results in the Table IV. The first one is related to  $(n_b/n_0)$ , as these values are very close to one, i.e., the saturation density. Thus, the phase transition is highly improbable at this point.

The second caveat concerns the baryon chemical potential. If we assume that the phase transition must occur for  $\mu_B > 1050$  MeV according to the Polyakov loop formalism, this condition is not satisfied here.

In Table V, one can see the similarities in values ( $G_v, B^{1/4}$ ) between  $H2 - EL3\omega\rho$  and  $H2 - NL3^*\omega\rho$ . Comparing the maximum values for mass, radius,  $C_s^2$ ,  $R_{1.4}$ , and  $\Lambda_{1.4}$  with the current observational margin of error for these measurements, it is natural to conclude that both models would describe the observations, except for the point of phase transition and the inconsistency of the nuclear parametrization set  $NL3^*\omega\rho$  with predictions from  $\chi EFT$  at low densities. These similarities also occur for  $H3 - EL3\omega\rho$  and  $H3 - NL3^*\omega\rho$ . Additionally, the parameter set obtained through Bayesian inference satisfies the instability condition for matter composed of u, d, and s quarks, as illustrated in Fig. 5(a) of Ref. [67]. A similar conclusion is presented in Fig. 4 of Ref.[10]. Moreover, when considering the Dirac sea contribution of the quarks

TABLE IV: Phase transition properties obtained from Bayesian inference with no constraints on the baryon density number.

Set	$n_b$ [ $1/\text{fm}^3$ ] ( $n_b/n_0$ ), $n_0 = 0.15$ [ $1/\text{fm}^3$ ]	$P_{\text{critical}}$ [ $\text{MeV}/\text{fm}^3$ ]	$\Delta\varepsilon$ [ $\text{MeV}/\text{fm}^3$ ]	$\mu_{\text{critical}}$ [ $\text{MeV}$ ]
H2(0.25, 153.51) - $EL3\omega\rho$	0.168 (1.12)	3.749	114.45	977.72
H3(0.26, 153.47, 0.98) - $EL3\omega\rho$	0.176 (1.17)	4.25	107.24	980.67
H2(0.25, 153.01) - $NL3^*\omega\rho$	0.158 (1.05)	2.47	117.10	969.33
H3(0.26, 152.68, 0.99) - $NL3^*\omega\rho$	0.161 (1.07)	2.68	112.50	970.69

TABLE V: Maximum values for mass, radius, speed of sound,  $\Lambda_{1.4}$ , and  $R_{1.4}$  for the inferred sets.

Parameter set	$M_{\text{max}}[M_{\odot}]$	$R_{\text{max}}[km]$	$c_s^2(\text{max})$	$\Lambda_{1.4}$	$R_{1.4}[km]$
H2(0.25, 153.51) - $EL3\omega\rho$	2.17	11.32	0.49	230	11.94
H3(0.26, 153.47, 0.98) - $EL3\omega\rho$	2.15	11.40	0.44	243	12.00
H2(0.25, 153.01) - $NL3^*\omega\rho$	2.18	11.59	0.49	184	11.74
H3(0.26, 152.68, 0.99) - $NL3^*\omega\rho$	2.17	11.36	0.44	195	11.81

in the vector channel, Fig. 7 of Ref. [10] demonstrates that the obtained parameters ( $G_v, B^{1/4}, b_4$ ) are also consistent with the *instability condition*. The inclusion of the Dirac sea contribution in the vector channel, as pointed out by the authors[10], softens the EoS at high densities. Thus, it is possible to have higher values of  $G_v$  while at the same time not increasing the baryon chemical potential for a fixed bag value.

The previous results show that even though the observational data agree with the inferred hybrid EoSs, the assumptions for the onset of phase transition conditions are not satisfied.

To prevent the baryon number density from being too close to the saturation density, we imposed, as done by the authors in Ref. [5], that it must be greater than  $1.5n_0$ .

Then, the following results for the parameter set  $EL3\omega\rho$  assuming  $n_B > 1.5n_0$ , are presented below

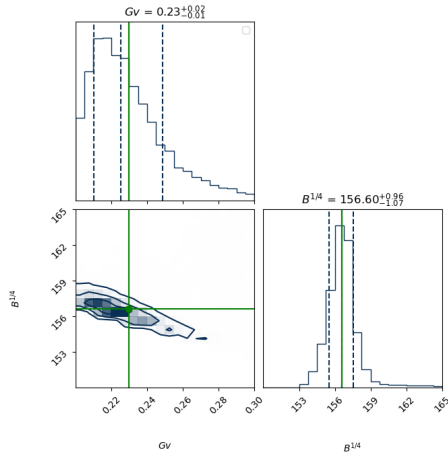


FIG. 11: The same plot as Fig. 1, but the phase transition is permitted only at densities greater than  $1.5n_0$  and with H2(0.23, 156.60) for the parameter set  $EL3\omega\rho$ .

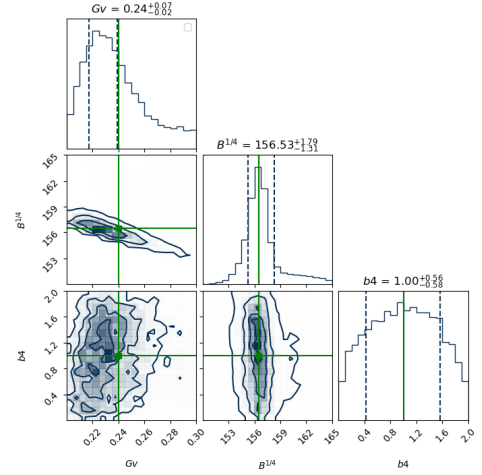


FIG. 12: The same plot as Fig. 6, but the phase transition is permitted only at densities greater than  $1.5n_0$  and with H3(0.24, 156.53, 1.0) for the parameter set  $EL3\omega\rho$ .

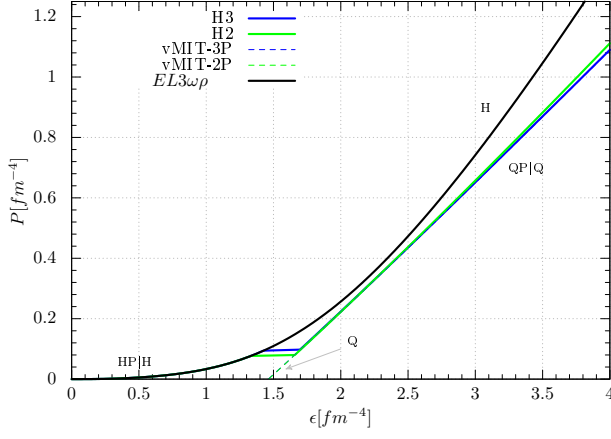


FIG. 13: The same plot as in Fig. 3, but the phase transition is permitted only at densities greater than  $1.5n_0$  and with H2(0.23, 156.60) and H3(0.24, 156.53, 1.0) for the parameter set  $EL3\omega\rho$ .

As expected, the critical pressures in Fig.13 for H2(0.23,156.60) and H3(0.24,156.53,1.0) are greater than those in Fig. 3. Moreover, the baryon chemical potential for the onset of phase transition, now, are  $\geq 1029\text{MeV}$ .

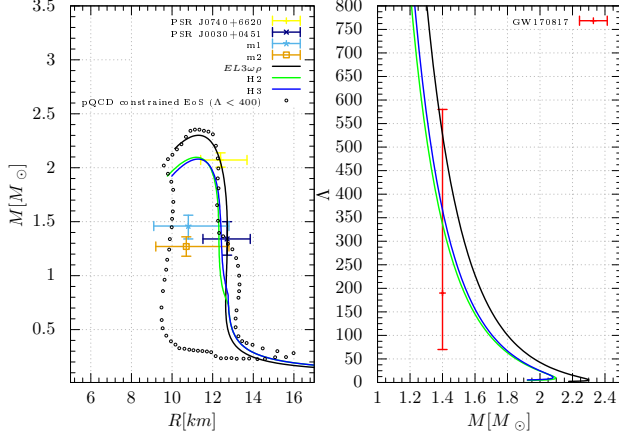


FIG. 14: The same plot as in Fig. 4, but the phase transition is permitted only at densities greater than  $1.5n_0$  and with H2(0.23, 156.60) and H3(0.24, 156.53, 1.0) for the parameter set  $EL3\omega\rho$ .

The  $M \times R$  relation for both sets in Fig. 14 is similar to the nuclear case for the EoS  $EL3\omega\rho$ . What favors the hybrid star are the values of the dimensionless tidal deformability, which are closer to the median value of the event GW170817.

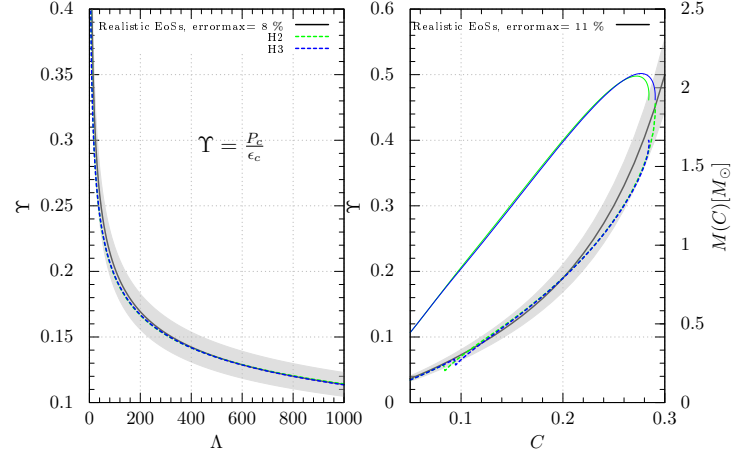


FIG. 15: The same plot as in Fig. 5, but the phase transition is permitted only at densities greater than  $1.5n_0$  and with H2(0.23, 156.60) and H3(0.24, 156.53, 1.0) for the parameter set  $EL3\omega\rho$ .

In the two plots in Fig. 15, both sets are within the error band for each approximate universal relation, i.e.,  $\Upsilon - \Lambda$  and  $\Upsilon - C$ . The H2(0.23,156.60) and H3(0.24,156.53,1.0) values for  $\Upsilon - \Lambda$  are basically the same as the median value from the fit.

The relation  $\Upsilon - C$  shows a slight disagreement for low  $C$  due to the phase transition, but above this point, both sets are also within the error band.

Thus, we can safely obtain the values for the dimensionless moment of inertia ( $\tilde{I}$ ) for our  $\Upsilon$  from sets H2(0.23,156.60) and H3(0.24,156.53,1.0) without the need to calculate the moment of inertia numerically.

The constraint on the onset of the phase transition improved two parameters: namely, the baryon number density and the critical chemical potential. Both values are more consistent with our previous assumptions. The set H3(0.24, 156.53, 1.0) shows the onset of the phase transition at  $1.93n_0$  with a critical baryon chemical potential of 1042 MeV, which is close to the value suggested by the Polyakov formalism, namely 1050 MeV.

The difference between the set H2(0.23,156.60) and the set H3(0.24,156.53,1.0) in terms of macroscopic features and tidal deformability is almost indistinguishable, as shown in Table VI. The set H3(0.24,156.53,1.0) exhibits a smaller reduction in the maximum mass and maximum speed of sound (indicating a less stiff EoS) and an increase in the dimensionless tidal deformability. When comparing these results with the current error estimations from observational data, it is not possible to favor one set over the other.

It is useful to analyze the case when the EoS also contains hyperons, since their presence softens the EoS. In this way, we consider the baryon octet and perform the same analyses with regard to the observed data for the parametrization set  $EL3\omega\rho Y$ .

TABLE VI: Phase transition properties obtained from Bayesian inference with a constraint on the baryon number density, i.e., allowing only density transitions greater than  $1.5n_0$

Set	$n_b$ [ $1/\text{fm}^3$ ] ( $n_b/n_0$ ), $n_0 = 0.15$ [ $1/\text{fm}^3$ ]	$P_{\text{critical}}$ [ $\text{MeV}/\text{fm}^3$ ]	$\Delta\varepsilon$ [ $\text{MeV}/\text{fm}^3$ ]	$\mu_{\text{critical}}$ [ $\text{MeV}$ ]
H2(0.23, 156.60) - $EL3\omega\rho$	0.272 (1.81)	15.50	62.33	1029
H3(0.24, 156.53, 1.0) - $EL3\omega\rho$	0.290 (1.93)	19.01	51.10	1042

TABLE VII: Maximum values for mass, radius, speed of sound,  $\Lambda_{1.4}$ , and  $R_{1.4}$  for the inferred sets.

Set	$M_{\text{max}}$ [ $M_{\odot}$ ]	$R_{\text{max}}$ [ $\text{km}$ ]	$c_s^2(\text{max})$	$\Lambda_{1.4}$	$R_{1.4}$ [ $\text{km}$ ]
H2(0.23,156.60) - $EL3\omega\rho$	2.09	11.20	0.49	336.19	12.29
H3(0.24,156.53,1.0) - $EL3\omega\rho$	2.08	11.29	0.44	369.91	12.42

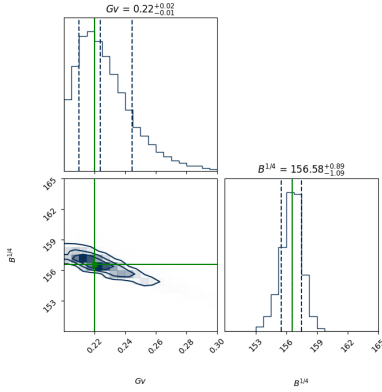


FIG. 16: The same plot as Fig. 1, but the phase transition is permitted only at densities greater than  $1.5n_0$  and with H2(0.22,156.58) for the parameter set  $EL3\omega\rho Y$ .

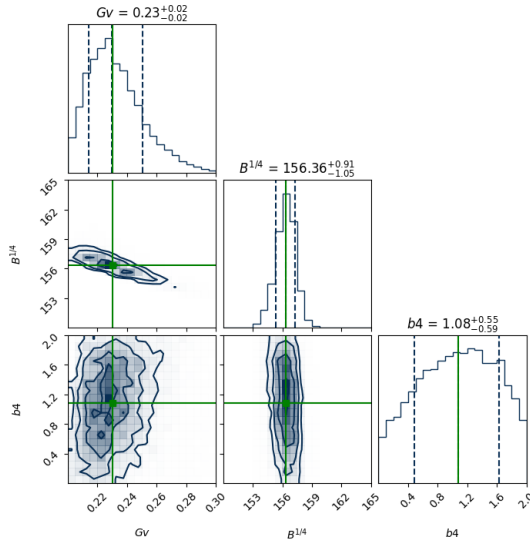


FIG. 17: The same plot as Fig. 6, but the phase transition is permitted only at densities greater than  $1.5n_0$  and with H3(0.23,156.36,1.08) for the parameter set  $EL3\omega\rho Y$ .

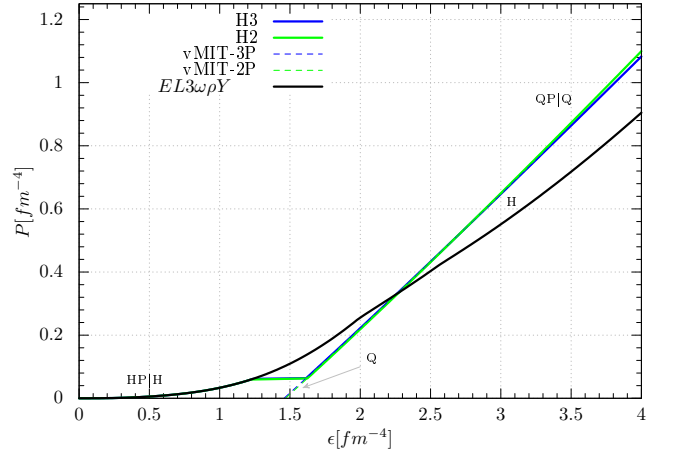


FIG. 18: The same plot as in Fig. 3, but the phase transition is permitted only at densities greater than  $1.5n_0$  and with H2(0.22,156.58) and H3(0.23,156.36,1.08) for the parameter set  $EL3\omega\rho Y$ .

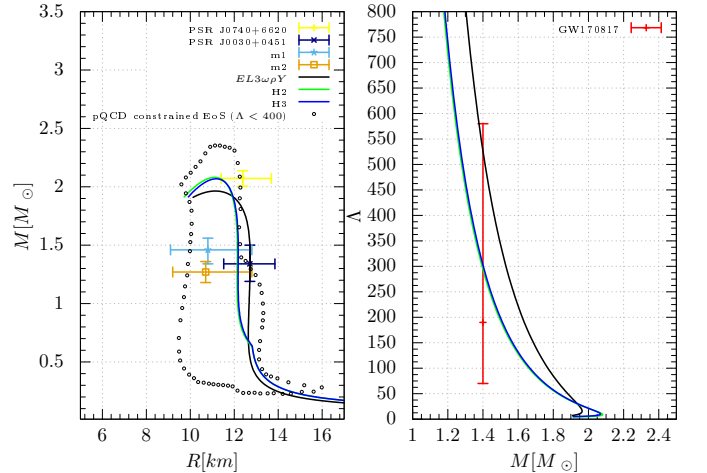


FIG. 19: The same plot as in Fig. 4, but the phase transition is permitted only at densities greater than  $1.5n_0$  and with H2(0.22,156.58) and H3(0.23,156.36,1.08) for the parameter set  $EL3\omega\rho Y$ .

In Fig. 19, in the left plot, the EoS with hyperons,  $EL3\omega\rho Y$ , has a maximum mass of around  $2 M_\odot$ . Meanwhile, the sets H2(0.22,156.58) and H3(0.23,156.36,1.08) yield essentially the same maximum mass and maximum radius as in the case without hyperons.

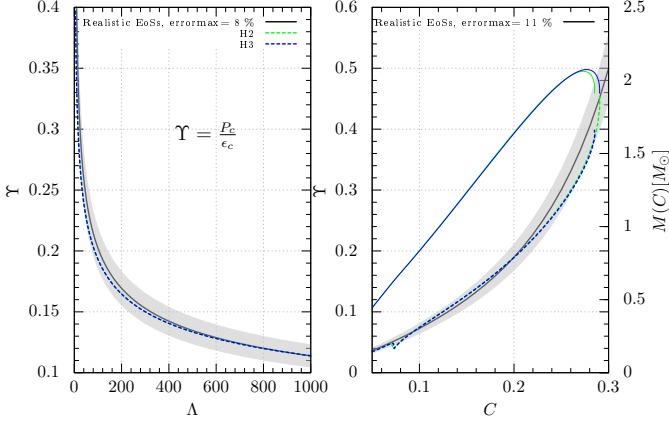


FIG. 20: The same plot as in Fig. 5, but the phase transition is permitted only at densities greater than  $1.5n_0$  and with H2(0.22,156.58) and H3(0.23,156.36,1.08) for the parameter set  $EL3\omega\rho Y$ .

In the approximate universal relation shown in Fig. 20, there is no significant difference compared to  $EL3\omega\rho$ , i.e., both lie within the error band for each relation. Thus, we can safely estimate  $\Upsilon - \bar{I}$ .

In Table VIII, one can see that the main differences compared to the case without hyperons,  $EL3\omega\rho$ , are the onset of the phase transition, i.e., it occurs closer to  $1.5n_0$ , and the values of the critical baryon chemical potential for both sets, which are indistinguishable and lower when compared to the best-case H3(0.24,156.53,1.0) without hyperons.

The density transition found in the Table VIII is before the appearance of  $\Lambda^0$ , as we can see in the Fig. 24 in the appendix a (item b) for the  $EL3\omega\rho Y$ .

The values presented in Table VII, i.e.,  $EL3\omega\rho$  for the set H2 and H3 are similar to those presented in Table IX. Therefore, based on the prediction of the Polyakov loop formalism, the inferred set with hyperons is less probable than those without hyperons. In this way, we consider the set H3(0.24,156.53,1.0) -  $EL3\omega\rho$  as the most probable.

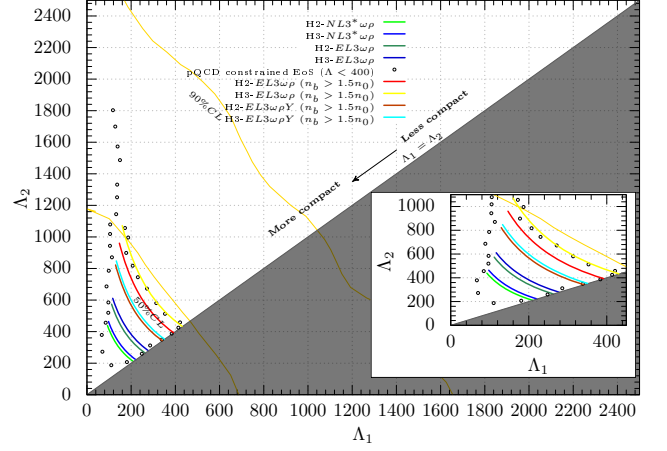


FIG. 21: The plot of  $\Lambda_1$  against  $\Lambda_2$  is shown for both vMIT inferences for the parameter sets  $EL3\omega\rho$  and  $NL3^*\omega\rho$  with and without the density transition phase. The results show that hybrid stars have a 50% credible interval to describe the event GW170817 for low-spin priors.

In Fig. 21, the inferred sets for the onset of the phase transition with  $n_B > 1.5n_0$  are less compact than those with  $n_B < 1.5n_0$ . Nevertheless, regarding  $\Lambda_1 \times \Lambda_2$ , all inferred sets lie within the prediction of the pQCD constrained EoS.

Finally, to estimate the order of the quark phase, the gravitational mass of the quark phase, and the baryonic mass of the quark phase, we calculate them only for the phase transition with  $n_B > 1.5n_0$  using  $EL3\omega\rho$  and  $EL3\omega\rho Y$ , since these provide our best results. These results correspond to the most massive star in the stellar sequence.

In Fig. 22, we show the gravitational mass in terms of the internal radius for the inferred set. One can notice that all pf them have large quark cores, since  $R_{\text{quark}} > 6$  km.

In Table X, we quantify the ratio of gravitational quark mass, baryonic quark mass, and quark radius in terms of the total mass and total radius for the inferences with the phase constraint  $n_B > 1.5n_0$ .

As we can see in Table X, the presence of hyperons makes the quark phase larger than the nuclear phase with no hyperons. This can be explained by the phase transition onset occurring earlier. Nonetheless, these results are similar to those of the authors of [23], who found both the gravitational quark mass and the quark core radius to be greater than 80% of the hybrid star.

We also performed a Bayesian inference for the constraints used by the authors [68] to compare the quark size and its radius. We applied the parameter set  $EL3\omega\rho$  for three parameters and found H3(0.23,157.09,0.99). This resulted in a maximum mass of  $2.06 M_\odot$ , a maximum radius of 11.16 km,  $R_{1.4} = 12.28$  km, a maximum

TABLE VIII: Phase transition properties obtained from Bayesian inference with a constraint on the baryon number density, i.e., allowing only density transitions greater than  $1.5n_0$

Set	$n_b$ [ $1/\text{fm}^3$ ] ( $n_b/n_0$ ), $n_0 = 0.15$ [ $1/\text{fm}^3$ ]	$P_{\text{critical}}$ [ $\text{MeV}/\text{fm}^3$ ]	$\Delta\varepsilon$ [ $\text{MeV}/\text{fm}^3$ ]	$\mu_{\text{critical}}$ [ $\text{MeV}$ ]
H2(0.22, 156.58) - $EL3\omega\rho Y$	0.251 (1.67)	12.13	76.16	1017
H3(0.23, 156.36, 1.08) - $EL3\omega\rho Y$	0.254 (1.69)	12.58	71.63	1018

TABLE IX: Maximum values for mass, radius, speed of sound,  $\Lambda_{1.4}$ , and  $R_{1.4}$  for the inferred sets.

Set	$M_{\text{max}}$ [ $M_\odot$ ]	$R_{\text{max}}$ [ $\text{km}$ ]	$c_s^2(\text{max})$	$\Lambda_{1.4}$	$R_{1.4}$ [ $\text{km}$ ]
H2(0.22,156.58) - $EL3\omega\rho Y$	2.08	11.09	0.48	293.77	12.13
H3(0.23,156.36,1.08) - $EL3\omega\rho Y$	2.06	11.19	0.44	302.02	12.18

speed of sound of 0.44, and  $\Lambda_{1.4} = 356.22$ . The phase transition parameters are  $0.29 \text{ fm}^{-3}$  for the density transition and  $\mu_{\text{critical}} = 1043.8 \text{ MeV}$ . This result is similar to  $H3(0.23, 156.36, 1.08)$ .

It is important to note that the only constraints used here were  $1.97 \pm 0.04 M_\odot$  [69] and GW170817 ( $\Lambda_{1.4}$ ) [44]. In Fig. 3 from [68], for a hybrid star with  $2.0 M_\odot$ , the authors found  $\frac{M_{QG}}{M_{TOVG}} = 35\%$ ,  $\frac{R_Q}{R_{TOV}} = 54\%$ ,  $c_s^2(\text{max}) < \frac{1}{3}$ . These results do not agree with ours, as presented in Table X. However, the authors [70] conducted a Bayesian inference using two EoS based on the relativistic mean-field approach. The soft QMF EoS [71], which does not include a quark core, predicts a neutron star with a maximum mass of  $M = 2.07 M_\odot$  and a radius of  $R_{1.4} = 11.77 \text{ km}$ . In contrast, the stiff DD2 EoS [72] yields a maximum mass of  $M = 2.42 M_\odot$  and a radius of  $R_{1.4} = 13.17 \text{ km}$ . For high-density quark matter, they used the constant-speed-of-sound (CSS) parametrization [73] and a phase transition described by the Maxwell construction. The following results were obtained using different likelihood functions for PSR J0740+6620 ( $M = 2.14_{-0.09}^{+0.10} M_\odot$ ), and for the GW170817 event with the CSS parametrization for the quark phase. Thus, the comparison should be made carefully and in a more general manner. The results similar to H3(0.24,156.53,1.0) were those related to QMF+CSS, referred to as " + GW170817 + NICER", which are  $n_b = 0.32_{-0.13}^{+0.19} \text{ fm}^{-3}$ ,  $c_s^2(\text{max}) = 0.81_{-0.28}^{+0.17}$ ,  $M_{\text{max}} = 2.36_{-0.26}^{+0.49} M_\odot$ ,  $R_{\text{max}} = 10.96_{-1.01}^{+1.79} \text{ km}$ ,  $R_{1.4} = 11.70_{-0.74}^{+0.85} \text{ km}$ ,  $\Lambda_{1.4} = 312_{-124}^{+254}$ . They also found a large quark-core scenario, with  $R_{Q_{\text{core}}}/R_{TOV} \sim 90\%$ .

Calculating the difference between H3 (0.24, 156.53, 1.0) and the previous results, excluding the speed of sound and considering only median values, we obtain: (0.03  $\text{fm}^{-3}$ , 0.28  $M_\odot$ , 0.33 km, 0.59 km, 24.19). As a result, the maximum mass difference, 0.28  $M_\odot$ , can be considered the only significant difference in this comparison and can be attributed to two factors: the hadron-quark model and the likelihood function.

### A. Stability Against Radial Oscillations of Hybrid Stars

It is well known that the existence of a phase transition inside the neutron star could alter its stability properties. In fact there are two conditions to study the stability of a star. The first is the static stability condition, related to  $\partial M/\partial \epsilon_c \geq 0$  and the second case is the dynamical stability condition related to  $\omega > 0$ , where  $\omega$  is the frequency of the oscillation [74].

In this work we have considered the radial oscillations of hybrid stars, whose core is composed of deconfined quark matter and the external envelope is formed by hadronic matter. This two layer structure is produced by a phase transition inside the star. In principle we can classify those transitions as rapid or slow. Each type having a different effect on the oscillatory properties of the star. In the first case, i.e rapid transitions, the usual static stability condition  $\partial M/\partial \epsilon_c \geq 0$ , where  $\epsilon_c$  is the central density of a star whose total mass is  $M$ , remains always true. But in the case of a slow transition, the frequency that belongs to the fundamental mode can be a finite real number ( $\omega > 0$ ), which means stability, even for branches of the stellar models that verify the criterium  $\partial M/\partial \epsilon_c \leq 0$  (this generally happens after the point of maximum mass on the diagram  $M$  vs  $R$ ) [5, 74, 75].

For all of our models, considering slow phase transitions, we verified that beyond the point of maximum mass in the mass-radius diagrams, there exists a very small stellar branch satisfying  $\omega > 0$ . Therefore, in practical terms, the two conditions agree very well.

## VII. CONCLUSIONS

We investigated the phase transition characteristics from nuclear matter to deconfined quark matter inside hybrid stars by performing a Bayesian inference using the observational data in Table III to set the values in the likelihood functions. The prior ranges were defined

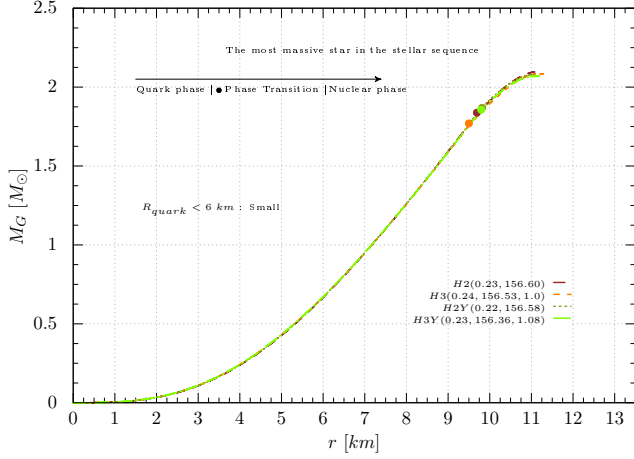


FIG. 22: We plot the inferred parameter set for the most massive star in the stellar sequence for both  $EL3\omega\rho$  and  $EL3\omega\rho Y$  in terms of gravitational mass. Here, H2 and H3 refer to models without hyperons, while H2Y and H3Y include hyperons.

In Fig. 22, we show the baryon mass in terms of the internal radius for the inferred set.

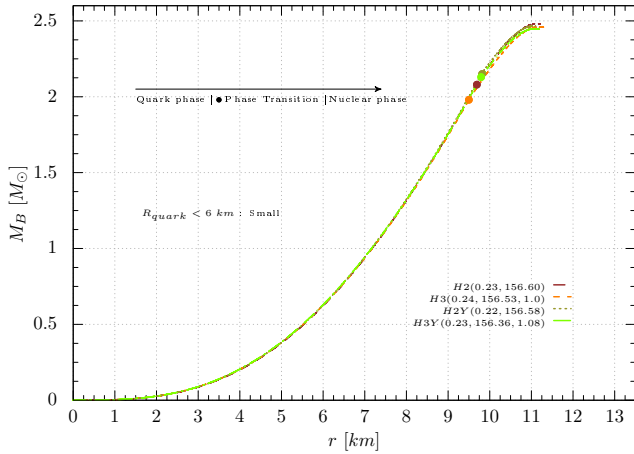


FIG. 23: We plot the inferred parameter set for the most massive star in the stellar sequence for both  $EL3\omega\rho$  and  $EL3\omega\rho Y$  in terms of baryon mass. Here, H2 and H3 refer to models without hyperons, while H2Y and H3Y include hyperons.

based on values reported in the literature. To model a first-order transition, the Maxwell construction was applied. The outer crust is modeled with the BPS EoS[12]. It is important to note that only the combination  $BPS-EL3\omega\rho$  lies within the uncertainties calculated with  $\chi$ EFT for densities below  $1.1n_0$ . Both parameter sets -  $NL3^*\omega\rho$  and  $EL3\omega\rho$  - individually describe the observations of PSR J0740+6620, PSR J0030+0451, and the gravitational event GW170817.

The inclusion of hyperons in  $EL3\omega\rho$  was also investigated.

To model the quark phase, the vMIT model was used with the free parameters  $G_v$ ,  $B^{1/4}$ , and  $b_4$ . Thus, each

combination of these parameters, along with the nuclear EoSs, produces a hybrid star if the conditions for phase coexistence are met, resulting in a posterior probability. The first results yielded, see Table IV, despite satisfying the observational constraints and the pQCD-constrained EoS ( $\Lambda < 400$ ), a phase transition near saturation density with  $\mu_{\text{critical}}$  well below the constraint from the Polyakov formalism, which states that the phase transition should have  $\mu_{\text{critical}} > 1050$  MeV.

An analysis was also performed using the approximate universal relations  $\Upsilon - \Lambda$  and  $\Upsilon - C$ , and the results were compared to the fit found by the authors [51]. Only the H2(0.25, 153.51) -  $EL3\omega\rho$  and H3(0.26, 153.47, 0.98) -  $EL3\omega\rho$  models can be used to approximately estimate the  $\Upsilon - \bar{I}$  relation, since they are within the error band of both  $\Upsilon - \Lambda$  and  $\Upsilon - C$ .

The results for dimensionless tidal deformability  $\Lambda_1 \times \Lambda_2$  for all results presented here are within the 50% credible interval to describe the event GW170817 for low-spin priors.

In the second set of results, see Table VI, we constrained the onset of the phase transition to be above  $1.5n_0$ . Both results, H2(0.23, 156.60) -  $EL3\omega\rho$  and H3(0.24, 156.53, 1.0) -  $EL3\omega\rho$ , improved  $\mu_{\text{critical}}$  as well as the  $\Upsilon - \Lambda$  and  $\Upsilon - C$  relations. Special attention is given to H3(0.24, 156.53, 1.0) -  $EL3\omega\rho$ , which has the onset of the phase transition at  $1.93n_0$  and  $\mu_{\text{critical}} = 1042$  MeV. These results are also within the  $M \times R$  and  $\Lambda_1 \times \Lambda_2$  open dots, which delimit the pQCD-constrained EoS ( $\Lambda < 400$ ).

The inclusion of the baryon octet in  $EL3\omega\rho$  alone does not allow it to reach the mass of PSR J0740+6620. Nevertheless, the hybrid stars with hyperons resulted in H2(0.22, 156.58) -  $EL3\omega\rho Y$  and H3(0.23, 156.36, 1.08) -  $EL3\omega\rho Y$ , which exhibit similar macroscopic features to the case without hyperons, see Table IX. The two main differences are the onset of the phase transition and  $\mu_{\text{critical}}$ . These values are nearly equal, with  $\sim 1.69n_0$  and  $\sim 1018$  MeV, respectively. We argue that these results are valid, since  $\mu_{\text{critical}}$  is close to 1050 MeV.

Furthermore, we calculated the gravitational mass of quark core, the baryon mass of quark core and the radius of quark core. We found that for both hybrid star with  $EL3\omega\rho$  and  $EL3\omega\rho Y$ , the quark core size composes 80% of the hybrid star. The same goes for gravitational mass and baryon mass of the quark core. These results are in agreement with those found by the authors [23, 70].

An additional test was implemented for all hybrid stars, i.e., radial oscillations for both rapid and slow transitions, and it was found that these stars satisfied both conditions.

Finally, comparing our best result, H3 (0.24, 156.53, 1.0)- $EL3\omega\rho$ , with those related to QMF+CSS [70], the onset of the phase transition is almost the same. The difference between  $R_{\max}$  and  $R_{1.4}$  is less than 0.6 km, and the dimensionless tidal deformability differs by 24.9. Only the maximum mass,  $M_{\max}$ , shows a considerable difference of  $0.28 M_{\odot}$ , which may be attributed to the hadron-quark model and the likelihood function.

A similar study on the phase transition in hybrid stars was conducted by the authors [76]. They employed a relativistic mean field hadronic model the BMPF 220 parameterization (soft EoS) for the hadronic phase and mean field theory QCD (MFTQCD) for the quark phase. Their analysis was based on the pulsars PSR J0030+0451 and PSR J0740+6620, with two additional constraints imposed on the phase transition and the limit of pQCD. Their results, both with and without pQCD constraints, were similar to those we obtained for H2(0.23, 156.60) –  $EL3\omega\rho$  and H3(0.24, 156.53, 1.0) –  $EL3\omega\rho$ . They found the following mean values:  $M_{\max} = 2.101 M_{\odot}$ ,  $n_b(\text{transition}) = 0.259 \text{ fm}^{-3}$ ,  $R_{\max} = 11.27 \text{ km}$ ,  $c_s^2(\text{max}) = 0.488$ ,  $R_{1.4} = 12.42 \text{ km}$ . Comparing these values with those shown in Tables VI and VII, one can notice that they are almost the same. This is due to similarities between MFTQCD and vMIT. Their results also partially describe the HESS observation. Furthermore, the Nambu-Jona-Lasinio (NJL) model yields phase transition median values ( $> 2n_0$ ) that are higher than those predicted by MFTQCD for both the soft and stiff EOS, and it cannot describe the HESS observation. For more details on MFTQCD, see Refs. [76–78].

We conclude that our analysis has improved the understanding of the phase transition in hybrid stars, since our results are in good agreement with QMF+CSS (agnostic EoS) [70] and BMPF 220+MFTQCD. In other words,  $EL3\omega\rho + v\text{MIT}$  indicates a phase transition below  $2n_0$  and satisfies the constraints in Table III as well as the pQCD constraints, without the need to include it in the Bayesian analysis. The small differences compared to BMPF 220+MFTQCD can be attributed to the minor differences in the quark masses (MFTQCD), the MFTQCD model itself, and the parametrization of BMPF 220.

## ACKNOWLEDGEMENTS

This work is a part of the project INCT-FNA proc. No. 408419/2024-5. It is also supported by Conselho Nacional de Desenvolvimento Científico e Tecnológico (CNPq) under Grant No. 303490/2021-7 (D.P.M.). F.K would like to thank FAPESC/CNPq for financial support

under grants 174332/2023-8.

## VIII. APPENDIX A

### A. Hyperon-Meson Coupling

The hyperons included in the  $EL3\omega\rho Y$  model are  $\Lambda, \Sigma^-, \Sigma^0, \Sigma^+, \Xi^-,$  and  $\Xi^0$ . Only one hyperon-meson coupling is well established, which is related to  $\Lambda^0$  and has a potential depth of  $U_\Lambda = -28$  MeV. For the remaining hyperons, the vector mesons are constrained by the SU(6) symmetry group [79]. However, for the scalar mesons [80, 81], we consider the following potential depths:  $U_\Sigma = 30$  MeV and  $U_\Xi = -4$  MeV. These potentials are in good agreement with those extracted from LQCD for hyperon interactions [82]. The hyperon masses are taken as  $m_\Lambda = 1116$  MeV,  $m_\Sigma = 1193$  MeV,  $m_\Xi = 1318$  MeV while  $M = 939$  MeV and  $m_\phi = 1020$  MeV. The full Lagrangian for the baryon octet can be found in [29].

The hyperon-meson couplings according to SU(6) are:

$$\frac{g_{\Lambda\omega}}{g_{N\omega}} = \frac{2}{3}, \quad \frac{g_{\Sigma\omega}}{g_{N\omega}} = \frac{2}{3}, \quad \text{and} \quad \frac{g_{\Xi\omega}}{g_{N\omega}} = \frac{1}{3}, \quad (26)$$

for hyperon- $\omega$  meson couplings.

$$\frac{g_{\Lambda\phi}}{g_{N\omega}} = \frac{-\sqrt{2}}{3}, \quad \frac{g_{\Sigma\phi}}{g_{N\omega}} = \frac{-\sqrt{2}}{3}, \quad \text{and} \quad \frac{g_{\Xi\phi}}{g_{N\omega}} = \frac{-2\sqrt{2}}{3}, \quad (27)$$

for hyperon- $\phi$  meson couplings.

$$\frac{g_{\Lambda\rho}}{g_{N\rho}} = 0, \quad \frac{g_{\Sigma\rho}}{g_{N\rho}} = 2, \quad \text{and} \quad \frac{g_{\Xi\rho}}{g_{N\rho}} = 1. \quad (28)$$

for hyperon- $\rho$  meson couplings.

While those based on potential depths:

$$\frac{g_{\Lambda\sigma}}{g_{N\sigma}} = 0.610, \quad \frac{g_{\Sigma\sigma}}{g_{N\sigma}} = 0.406, \quad \text{and} \quad \frac{g_{\Xi\sigma}}{g_{N\sigma}} = 0.269. \quad (29)$$

for hyperon- $\sigma$  meson couplings. One can note that  $g_{N\phi} = 0$ .

The particle fraction and speed of sound as a function of the baryon number density for the  $EL3\omega\rho Y$  parametrization are given by

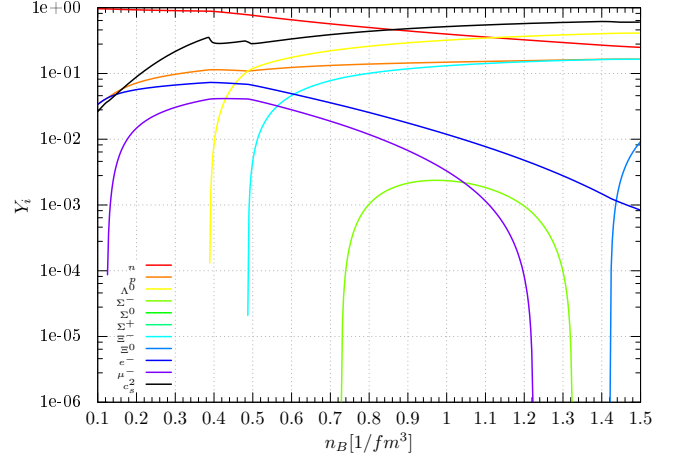


FIG. 24: Particle fraction and speed of sound as a function of the baryon number density for the  $EL3\omega\rho Y$  parametrization.

The appearance of  $\Lambda^0$  and  $\Xi^-$  significantly reduces the speed of sound ( $c_s^2$ ), while the appearance of  $\Xi^0$  at high densities leads to a slight reduction in the speed of sound.

### B. Ratios

- 
- [1] B. P. Abbott, R. Abbott, T. D. Abbott, and et al. (The LIGO Scientific Collaboration and the Virgo Collaboration), *Phys. Rev. Lett.* **121**, 161101 (2018).
  - [2] T. E. Riley, A. L. Watts, P. S. Ray, S. Bogdanov, S. Guillot, S. M. Morsink, A. V. Bilous, Z. Arzoumanian, D. Choudhury, J. S. Deneva, *et al.*, *The Astrophysical Journal Letters* **918**, L27 (2021).
  - [3] M. C. Miller *et al.*, *Astrophys. J. Lett.* **887**, L24 (2019), [arXiv:1912.05705 \[astro-ph.HE\]](#).
  - [4] M. C. Miller *et al.*, *Astrophys. J. Lett.* **918**, L28 (2021), [arXiv:2105.06979 \[astro-ph.HE\]](#).
  - [5] M. Mariani, I. F. Ranea-Sandoval, G. Lugones, and M. G. Orsaria, *Phys. Rev. D* **110**, 043026 (2024), [arXiv:2407.06347 \[astro-ph.HE\]](#).
  - [6] S. M. A. Imam, N. K. Patra, C. Mondal, T. Malik, and B. K. Agrawal, *Phys. Rev. C* **105**, 015806 (2022), [arXiv:2110.15776 \[nucl-th\]](#).
  - [7] T. Malik, B. K. Agrawal, and C. Providência, *Phys. Rev. C* **106**, L042801 (2022), [arXiv:2206.15404 \[nucl-th\]](#).
  - [8] M. W. Coughlin and T. Dietrich, *Phys. Rev. D* **100**, 043011 (2019), [arXiv:1901.06052 \[astro-ph.HE\]](#).
  - [9] N. K. Glendenning, *Phys. Rev. D* **46**, 1274 (1992).
  - [10] L. L. Lopes, C. Biesdorf, and D. e. P. Menezes, *Phys. Scripta* **96**, 065303 (2021), [arXiv:2005.13136 \[hep-ph\]](#).
  - [11] J. Boguta and A. R. Bodmer, *Nuclear Physics A* **292**, 413 (1977).
  - [12] G. Baym, C. Pethick, and P. Sutherland, *The Astrophysical Journal* **170**, 299 (1971).
  - [13] J. D. Walecka, *Annals of Physics* **83**, 491 (1974).
  - [14] L. L. Lopes and D. P. Menezes, *Astrophys. J.* **936**, 41 (2022), [arXiv:2111.02247 \[hep-ph\]](#).
  - [15] L. L. Lopes, *Commun. Theor. Phys.* **74**, 015302 (2022), [arXiv:2107.02245 \[hep-ph\]](#).
  - [16] M. Dutra, O. Lourenço, S. S. Avancini, B. V. Carlson,

Set ( $EL3\omega\rho$ )	Gravitational Mass - $M_{Q_{core}}/M_{TOV}$ (%)	Baryonic Mass - $M_{Q_{core}}/M_{TOV}$ (%)	Ratio Radius - $R_{Q_{core}}/R_{TOV}$ (%)
H2(0.23, 156.60)	1.83/2.09 (87%)	2.08/2.48 (83%)	9.69/11.20 (86%)
H3(0.24, 156.53, 1.0)	1.77/2.08 (85%)	1.98/2.45 (80%)	9.50/11.29 (84%)
Set ( $EL3\omega\rho Y$ )	-	-	-
H2(0.22, 156.58)	1.87/2.08 (89%)	2.15/2.46 (87%)	9.81/11.09 (88%)
H3(0.23, 156.36, 1.08)	1.86/2.06 (90%)	2.13/2.44 (87%)	9.79/11.19 (87%)

TABLE X: Ratios between the quark core and TOV solutions.

- A. Delfino, D. P. Menezes, C. Providência, S. Typel, and J. R. Stone, *Physical Review C* **90**, 055203 (2014).
- [17] A. R. Bodmer, *Phys. Rev. D* **4**, 1601 (1971).
- [18] H. Terazawa, *J. Phys. Soc. Jap.* **58**, 3555 (1989).
- [19] E. Witten, *Phys. Rev. D* **30**, 272 (1984).
- [20] K. Nagata, *Prog. Part. Nucl. Phys.* **127**, 103991 (2022), [arXiv:2108.12423 \[hep-lat\]](#).
- [21] H. Heiselberg and V. Pandharipande, *Ann. Rev. Nucl. Part. Sci.* **50**, 481 (2000), [arXiv:astro-ph/0003276](#).
- [22] A. Chodos, R. L. Jaffe, K. Johnson, C. B. Thorn, and V. F. Weisskopf, *Physical Review D* **9**, 3471 (1974).
- [23] L. L. Lopes, C. Biesdorf, and D. P. Menezes, *Monthly Notices of the Royal Astronomical Society* **512**, 5110 (2022).
- [24] C. A. Graeff, M. D. Alloy, K. D. Marquez, C. Providência, and D. P. Menezes, *Journal of Cosmology and Astroparticle Physics* **2019** (01), 024.
- [25] K. D. Marquez and D. P. Menezes, *Journal of Cosmology and Astroparticle Physics* **2017** (12), 028.
- [26] Y. Aoki, G. Endrődi, Z. Fodor, S. D. Katz, and K. K. Szabó, *Nature* **443**, 675 (2006).
- [27] R. Bellwied, S. Borsányi, Z. Fodor, J. Günther, S. Katz, C. Ratti, and K. Szabo, *Physics Letters B* **751**, 559 (2015).
- [28] X. Luo, S. Shi, N. Xu, and Y. Zhang, *Particles* **3**, 278 (2020).
- [29] C. Biesdorf, D. P. Menezes, and L. L. Lopes, *Braz. J. Phys.* **53**, 137 (2023), [arXiv:2303.10734 \[hep-ph\]](#).
- [30] A. Bazavov, H.-T. Ding, P. Hegde, O. Kaczmarek, F. Karsch, E. Laermann, S. Mukherjee, H. Ohno, P. Petreczky, E. Rinaldi, *et al.*, *Physical Review D* **96**, 074510 (2017).
- [31] A. Bazavov, H.-T. Ding, P. Hegde, O. Kaczmarek, F. Karsch, E. Laermann, Y. Maezawa, S. Mukherjee, H. Ohno, P. Petreczky, *et al.*, *Physical Review D* **95**, 054504 (2017).
- [32] K. Fukushima and T. Hatsuda, *Reports on Progress in Physics* **74**, 014001 (2010).
- [33] D. N. Voskresensky, M. Yasuhira, and T. Tatsumi, *Nucl. Phys. A* **723**, 291 (2003), [arXiv:nucl-th/0208067](#).
- [34] T. Maruyama, S. Chiba, H.-J. Schulze, and T. Tatsumi, *Phys. Rev. D* **76**, 123015 (2007), [arXiv:0708.3277 \[nucl-th\]](#).
- [35] M. B. Pinto, V. Koch, and J. Randrup, *Phys. Rev. C* **86**, 025203 (2012), [arXiv:1207.5186 \[hep-ph\]](#).
- [36] G. Lugones, A. G. Grunfeld, and M. Al Ajmi, *Phys. Rev. C* **88**, 045803 (2013), [arXiv:1308.1452 \[hep-ph\]](#).
- [37] G. Lugones and A. G. Grunfeld, *Phys. Rev. C* **95**, 015804 (2017), [arXiv:1610.05875 \[nucl-th\]](#).
- [38] G. Lugones and A. G. Grunfeld, *Phys. Rev. C* **99**, 035804 (2019), [arXiv:1811.09954 \[astro-ph.HE\]](#).
- [39] J. R. Oppenheimer and G. M. Volkoff, *Phys. Rev.* **55**, 374 (1939).
- [40] T. Damour and A. Nagar, *Phys. Rev. D* **80**, 084035 (2009).
- [41] T. Hinderer, B. D. Lackey, R. N. Lang, and J. S. Read, *Phys. Rev. D* **81**, 123016 (2010).
- [42] C. V. Flores, C. H. Lenzi, M. Dutra, O. Lourenço, and J. D. V. Arbañil, *Phys. Rev. D* **109**, 083021 (2024).
- [43] The properties of gravitational-wave sources are determined by comparing observational data with a post-Newtonian waveform model in the frequency domain. The collaboration[44] performs a Bayesian analysis across a frequency range of 302048 Hz.
- [44] B. P. Abbott *et al.* (LIGO Scientific, Virgo), *Phys. Rev. Lett.* **119**, 161101 (2017), [arXiv:1710.05832 \[gr-qc\]](#).
- [45] K. Yagi and N. Yunes, *Classical and Quantum Gravity* **33**, 13LT01 (2016).
- [46] R. B. Wiringa, V. Fiks, and A. Fabrocini, *Phys. Rev. C* **38**, 1010 (1988).
- [47] H. Mueller and B. D. Serot, *Nucl. Phys. A* **606**, 508 (1996), [arXiv:nucl-th/9603037](#).
- [48] J. M. Lattimer and F. D. Swesty, *Nucl. Phys. A* **535**, 331 (1991).
- [49] A. Akmal, V. Pandharipande, and D. Ravenhall, *Phys. Rev. C* **58**, 1804 (1998), [arXiv:nucl-th/9804027](#).
- [50] K. Yagi and N. Yunes, *Science* **341**, 365 (2013), <https://www.science.org/doi/pdf/10.1126/science.1236462>.
- [51] J. A. Saes and R. F. P. Mendes, *Phys. Rev. D* **106**, 043027 (2022), [arXiv:2109.11571 \[gr-qc\]](#).
- [52] T. Malik, M. Ferreira, B. K. Agrawal, and C. Providência, *Astrophys. J.* **930**, 17 (2022), [arXiv:2201.12552 \[nucl-th\]](#).
- [53] S. Wesolowski, N. Klco, R. J. Furnstahl, D. R. Phillips, and A. Thapaliya, *J. Phys. G* **43**, 074001 (2016), [arXiv:1511.03618 \[nucl-th\]](#).
- [54] R. J. Furnstahl, N. Klco, D. R. Phillips, and S. Wesolowski, *Phys. Rev. C* **92**, 024005 (2015), [arXiv:1506.01343 \[nucl-th\]](#).
- [55] G. Ashton *et al.*, *Astrophys. J. Suppl.* **241**, 27 (2019), [arXiv:1811.02042 \[astro-ph.IM\]](#).
- [56] C. Huang, G. Raaijmakers, A. L. Watts, L. Tolos, and C. Providência, *Mon. Not. Roy. Astron. Soc.* **529**, 4650 (2024), [arXiv:2303.17518 \[astro-ph.HE\]](#).
- [57] P. Char, C. Mondal, F. Gulminelli, and M. Oertel, *Phys. Rev. D* **108**, 103045 (2023), [arXiv:2307.12364 \[nucl-th\]](#).
- [58] S. M. A. Imam, T. Malik, C. Providência, and B. K. Agrawal, *Phys. Rev. D* **109**, 103025 (2024), [arXiv:2401.06018 \[nucl-th\]](#).
- [59] T. Bayes, *Philosophical Transactions of the Royal Society of London* **53**, 370 (1763).
- [60] T. Riley, A. Watts, S. Bogdanov, P. Ray, R. Ludlam, S. Guillot, Z. Arzoumanian, C. Baker, A. Bilous, D. Chakrabarty, *et al.*, *ApJL* **887**, L21 (2019).
- [61] D. Foreman-Mackey, D. W. Hogg, D. Lang, and J. Good-

- man, *Publications of the Astronomical Society of the Pacific* **125**, 306 (2013).
- [62] D. Foreman-Mackey, *The Journal of Open Source Software* **1**, 24 (2016).
- [63] T. Williams and C. Kelley and others, *Gnuplot: An Interactive Plotting Program* (2020), version 5.4, Available at <http://www.gnuplot.info>.
- [64] E. Annala, T. Gorda, A. Kurkela, and A. Vuorinen, *Phys. Rev. Lett.* **120**, 172703 (2018).
- [65] K. Hebeler and A. Schwenk, *Phys. Rev. C* **82**, 014314 (2010), [arXiv:0911.0483](https://arxiv.org/abs/0911.0483) [nucl-th].
- [66] A. Kurkela, P. Romatschke, and A. Vuorinen, *Phys. Rev. D* **81**, 105021 (2010).
- [67] P. Laskos-Patkos, P. S. Koliogiannis, and C. C. Moustakidis, *Phys. Rev. D* **109**, 063017 (2024), [arXiv:2312.07113](https://arxiv.org/abs/2312.07113) [astro-ph.HE].
- [68] E. Annala, T. Gorda, A. Kurkela, J. Nättilä, and A. Vuorinen, *Nature Phys.* **16**, 907 (2020), [arXiv:1903.09121](https://arxiv.org/abs/1903.09121) [astro-ph.HE].
- [69] P. Demorest, T. Pennucci, S. Ransom, M. Roberts, and J. Hessels, *Nature* **467**, 1081 (2010).
- [70] A. Li, Z. Miao, S. Han, and B. Zhang, *The Astrophysical Journal* **913**, 27 (2021).
- [71] Z.-Y. Zhu, E.-P. Zhou, and A. Li, *The Astrophysical Journal* **862**, 98 (2018).
- [72] M. Fortin, C. Providência, A. R. Raduta, F. Gulminelli, J. L. Zdunik, P. Haensel, and M. Bejger, *Phys. Rev. C* **94**, 035804 (2016).
- [73] M. G. Alford, S. Han, and M. Prakash, *Phys. Rev. D* **88**, 083013 (2013), [arXiv:1302.4732](https://arxiv.org/abs/1302.4732) [astro-ph.SR].
- [74] J. P. Pereira, C. V. Flores, and G. Lugones, *Astrophys. J.* **860**, 12 (2018), [arXiv:1706.09371](https://arxiv.org/abs/1706.09371) [gr-qc].
- [75] C. Vásquez Flores, C. H. Lenzi, and G. Lugones, in *International Journal of Modern Physics Conference Series*, International Journal of Modern Physics Conference Series, Vol. 18 (2012) pp. 105–108.
- [76] M. Albino, T. Malik, M. Ferreira, and C. Providência, *Phys. Rev. D* **110**, 083037 (2024), [arXiv:2406.15337](https://arxiv.org/abs/2406.15337) [nucl-th].
- [77] D. A. Fogaca and F. S. Navarra, *Phys. Lett. B* **700**, 236 (2011), [arXiv:1012.5266](https://arxiv.org/abs/1012.5266) [hep-ph].
- [78] B. Franzon, D. A. Fogaça, F. S. Navarra, and J. E. Horvath, *Phys. Rev. D* **86**, 065031 (2012).
- [79] A. Pais, *Rev. Mod. Phys.* **38**, 215 (1966).
- [80] L. L. Lopes and D. P. Menezes, *Nucl. Phys. A* **1009**, 122171 (2021), [arXiv:2004.07909](https://arxiv.org/abs/2004.07909) [astro-ph.HE].
- [81] L. L. Lopes, K. D. Marquez, and D. P. Menezes, *Phys. Rev. D* **107**, 036011 (2023), [arXiv:2211.17153](https://arxiv.org/abs/2211.17153) [hep-ph].
- [82] Hyperon forces from qcd and their applications, in *Proceedings of the 8th International Conference on Quarks and Nuclear Physics (QNP2018)*, <https://journals.jps.jp/doi/pdf/10.7566/JPSCP.26.023018>.